Supplement of Atmos. Chem. Phys., 25, 14987–15007, 2025
https://doi.org/10.5194/acp-25-14987-2025-supplement

Atmospheric Chemistry and Physics
Open Access
EGU

Supplement of

Enhancement of O_3–CO ratios at tropospheric subtropical latitudes: Photochemistry and stratospheric influence

Linda Ort et al.

Correspondence to: Linda Ort (linda.ort@mpic.de)

S1 Aircraft observations

The aircraft observations were taken from 12 different missions (ESMVal, OMO, WISE, ATom 1, ATom 2, ATom 3, ATom 4, CAFE Africa, SouthTRAC, CAFE Brazil, PHILEAS, CAFE Pacific) from 2012 to 2024, taking place in different locations and months. Additional information for each campaign and supporting material are presented below.

S1.1 The ESMVal campaign

The EMSVal (Earth System Model Validation) research phase took place in September 2012 and was carried out using the HALO research aircraft starting from its base at the German Aerospace center (DLR) in Oberpfaffenhofen, Germany, before circling the African continent. The campaign aimed to investigate the global climate–chemical–aerosol–cloud system and to validate numerical models. During the mission, several vertical profiles and a coverage of almost all latitudes from 80°S to 80°N could be achieved with seven research flights around the African and Europe continents. The ESMVal data sets are available on the HALO data base (DLR, 2012).

The CO concentrations have been measured with the tracer in situ TDLAS for atmospheric research (TRISTAR) spectrometer. This infrared spectrometer has been originally designed by Wienhold et al. (1998) but has been modified throughout the numerous campaigns which it has been used (Schiller et al., 2008; Tadic et al., 2017; Tomsche et al., 2019; Röder et al., 2024). For ESMVal, TRISTAR measured with alternating three-channel QCLS in the infrared range the absorption of CO, N_2O, and CH_4 through a 64-m-path multipass double corner cube White cell (White (1957); Wienhold et al. (1998)) with liquid-nitrogen-cooled detectors and lasers. For CO concentrations, one quantum cascade laser emitted at 2158.30 cm^{-1} and had a time resolution of 8 s (Müller et al., 2016). The total uncertainty of the CO measurements relative to the working standard during the ESMVal mission, including the instrumental drift between the calibration cycle every 30 minutes and the 2σ precision, is 1.8 ppbv overall (Schiller et al., 2008; Müller et al., 2016).

O_3 measurements were carried out with a dual-channel system instrument named FAIRO. This instrument combines two techniques to measure O_3 and thereby ensuring a high accuracy and high measurement frequency. FAIRO measures O_3 with UV photometry using light absorption at wavelengths between 250 and 260 nm and chemiluminescence (CL) detection at 254 nm (Hartley-Bande) (Zahn et al., 2012; Chiu et al., 2024). Under laboratory conditions the measurement uncertainties are 2 % for the UV photometry and 0.5 % for the CL detection with a time resolution up to 12.5 Hz. Due to the fact that the CL detection measures relative to the UV photometry as a continuous calibration, the overall measurement uncertainty of the data is 2.5 % (Rolf et al. (2015); Müller et al. (2016)). Further information can be found in Zahn et al. (2012).

S1.2 The OMO campaign

In July to August 2015, the OMO (Oxidation Mechanism Observations) mission took place in the upper troposphere over the eastern Mediterranean and the Arabian Peninsula. Over 18 research flights with the HALO research aircraft, the outflow of the South Asian summer monsoon was sampled and the influence on the Asian monsoon anticyclone was investigated (e.g., Tomsche et al. (2019); Hottmann et al. (2020)). The data sets of the OMO mission are available on the HALO data base (DLR, 2015).

The CO observations of the OMO campaign were measured with the TRISTAR instrument, the same QCLS instrument as introduced in Section S1.1. The averaged measurement uncertainty for CO over all flights, including drift behavior and precision of the instrument, is 5.1 % according to a certified reference gas with CO concentrations of 121.44 ± 1.46 ppbv (Tomsche et al., 2019).

The O_3 measurements were carried out with the FAIRO instrument with the same measurement uncertainty as already described above in Section S1.1. Unfortunately, during this campaign, the measurement uncertainty was influenced by a leak in the system and hence comes to approximated 10 %.

S1.3 The WISE campaign

In September and October 2017, the aircraft mission WISE (Wave-driven ISentropic Exchange) studied horizontal transport and mixing in the northern extra-tropical region over Iceland and exchange processes of the upper troposphere and lower stratosphere (UTLS). Based out of Shannon, Ireland, 15 research flights with the HALO research aircraft were carried out to investigate stratosphere–troposphere exchange processes with a number of trace gases and their horizontal and vertical gradients in the extra-tropical UTLS region through, e.g., planetary wave, Rossby wave breaking events, and their impact on cirrus cloud formation and radiative forcing (Riese and Hoor, 2017; Kunkel et al., 2019; Krasauskas et al., 2020; Bartolome Garcia et al., 2021). The WISE data sets can be accessed on the HALO data base (DLR, 2017).

CO measurements of WISE have been provided by the University of Mainz Airborne Quantum Cascade Laser-spectrometer (UMAQS), which is based on an Aerodyne Quantum Cascade Laser Mini Monitor (Aerodyne Research Inc, MA, USA) using direct absorption spectroscopy in a 76-m astigmatic multipass cell (McManus et al., 2010) with a continuous-wave quantum cascade laser to measure CO and N_2O with a sweep rate of 2 kHz, resulting in a temporal resolution of 1 Hz (Müller et al., 2015). The CO concentration is measured at an absorption wavelength of 2203.16 cm^{-1}. Frequent in-flight calibrations with a secondary standard assure stability and drift corrections during the measurements. The measurement uncertainty for CO is determined to be 0.94 ppbv for CO (Kunkel et al., 2019).

The O_3 measurements have been carried out with the FAIRO instrument with the same measurement uncertainty as already described above in Section S1.1.

S1.4 The ATom campaign

The NASA Atmospheric Tomography (ATom) mission (https://espo.nasa.gov/atom/, last access: 26 June 2024), operated by the NASA Armstrong (Dryden) Flight Research Center, aimed to collect in situ measurements of chemical components of the atmosphere in remote places over all seasons with the NASA DC-8 aircraft. The four campaign missions (ATom-1, -2, -3, -4)took place from 2016 to 2018 mostly over the ocean with a total of 47 scientific flights including several vertical profiles from 0.15 to 13 km with one mission in each season. For this study, the data of all ATom missions are used, which include ATom-1 (July–August 2016) (Strode et al., 2018), ATom-2 (January–February 2017), ATom-3 (September–November 2017), and ATom-4 (April–May 2018). Each mission started in Palmdale, California, and traversed the remote Pacific and Atlantic oceans, collecting various chemical and gas properties of the lower atmosphere over a wide range of latitudes. More information can be found in the overview article of the ATom campaign by Thompson et al. (2022). The ATom data sets are available on the ATom website (Wofsy et al., 2018).

The CO measurements used for this study were carried out with the Harvard QCLS instrument (Santoni et al., 2014). This QCLS instrument measures the absorption of CO at 2160 cm^{-1} with a pulsed quantum cascade laser through a 76-m-long astigmatic multi-pass cell and a liquid-nitrogen-cooled HgCdTe detector. The ATom CO concentration accuracy and precision are 3.5 and 0.15 ppbv, respectively (Strode et al., 2018), and it has a time resolution of 1 Hz.

The O_3 observations were sampled by the National Oceanic and Atmospheric Administration (NOAA) nitrogen oxides and ozone (NO_yO_3) instrument (Ridley et al., 1992). Besides other channels, the O_3 channel of this instrument uses CL detection together with the addition of pure NO as a reagent gas to measure ambient O_3 concentrations. The CL detection is calibrated on the ground and frequently during the flights with an independent instrument using UV optical absorption at 254 nm (Bourgeois et al., 2021). The NO_yO_3 instrument provides a total precision of 0.015 ppbv and a measurement uncertainty of 2 % of the O_3 data with a time resolution of 1 Hz (Bourgeois et al., 2020, 2021).

S1.5 The CAFE campaigns

The CAFE Africa and CAFE Brazil missions are part of three Chemistry of the Atmosphere Aircraft Observation (CAFE) missions, which aimed to understand chemical and dynamical processes in the tropical troposphere in more detail based on in situ measurements by the HALO aircraft. CAFE Africa was the first mission in August and September 2018 based in Sal on Capo Verde and covered with 14 research flights the northern tropical to subtropical region west of Africa. More information can

be found in Tadic et al. (2021). From December 2022 to January 2023 the second CAFE mission took place over the Amazon rainforest region based in Manaus, Brazil, including 16 local research flights and 4 transfer flights through Sal, Capo Verde. Here, the focus was on surface emissions, their transport and chemistry, and role in new particle formation in the free and upper troposphere. From January until February 2024, the third mission, CAFE Pacific, based in Cairns, Australia, was carried out above the Pacific northeast of Australia, as well as above the Australian continent. The data sets of the CAFE Africa, Brazil, and Pacific campaigns are available on the HALO data base (DLR, 2018, 2023a, 2024).

CO measurements were carried out with a further improved version of the TRISTAR instrument, introduced in Section S1.1. Since CAFE Africa, TRISTAR has been running on room-temperature lasers and detectors, which are stabilized by a 40°C – heating plate and the scanning and processing of the spectra are controlled digitally and no longer using analog technology. For CAFE Brazil, the alternating three-laser-system has been reduced to a single-laser-system providing continuous measurements on a 1-Hz frequency to gain more duty time for the gas of interest. Over all CAFE campaigns, frequent in-flight calibrations have been made with compressed air conditioned by a primary standard bottle with the standard errors given by the manufacturer (Luxfer Gas Cylinders Ltd., Colwick, Nottingham, England) with 0.36 ppbv for CO. CO measurements are provided with a temporal resolution of 10 s. Furthermore, another QCLS spectrometer, named ATTILA, measured CO simultaneously during the CAFE Brazil and CAFE Pacific campaigns (Ort et al., 2024). For this study, CO observations were taken from TRISTAR with a total measurement uncertainty of 4.3 % and 3.5 % for CAFE Africa and CAFE Brazil for 1 Hz data, respectively (Schiller et al., 2008; Ort et al., 2024; Röder et al., 2024). For CAFE Pacific, a combination of CO data from ATTILA and TRISTAR has been taken to cover all research flights. The mean measurement uncertainty is 5.3 % for the combination of TRISTAR and ATTILA CO measurements.

The O_3 measurements were carried out with the FAIRO instrument with the same measurement uncertainty as already described above in Section S1.1.

S1.6 The SouthTRAC campaign

From August to November 2019, the Southern Hemisphere Transport, Dynamics, and Chemistry (SouthTRAC) campaign based in Rio Grande, Argentina, measured over the course of 23 scientific flights the dynamical and chemical composition aspects of the Antarctic upper troposphere and gravity waves up to the mesosphere (Rapp et al., 2021). The mission was flown with the HALO aircraft and included four transfer flights from Oberpfaffenhofen, Germany, with a large zonal coverage. Altitudes up to 14.5 km could be reached. More information can be found on the SouthTRAC website (Rapp et al., 2019). The SouthTRAC data sets are available on the HALO data base (DLR, 2019).

CO measurements of SouthTRAC were also measured by the UMAQS instrument, described in Section S1.3. The CO measurements of the SouthTRAC campaign have a precision of 0.68 ppbv (2σ) and an accuracy of 1.22 ppbv, which results in a total uncertainty (relative to the secondary standard) of 1.4 ppbv (Müller et al., 2015).

The O_3 measurements were carried out with the FAIRO instrument with the same measurement uncertainty as already described above in section S1.1.

S1.7 The PHILEAS campaign

Probing high latitude export of air from the Asian summer monsoon was the research perspective of the PHILEAS campaign in summer 2023. The campaign was divided into two phases–one measuring the inflow of the Asian Summer Monsoon over Europe with the aircraft based in Oberpfaffenhofen, Germany and the second one based in Anchorage, Alaska, USA, to measure the long-range transported outflow of the Asian summer monsoon. In total, there were 18 research flights including 2 transfer flights with a fuel stop in Iceland. The PHILEAS data sets are available on the HALO data base (DLR, 2023b).

CO observations were carried out with the UMAQS instrument, which has been described in Section S1.3. The measurements uncertainty of CO is 0.32 ppbv with an accuracy of 0.64 ppbv.

The O_3 measurements were carried out with the FAIRO instrument with the same measurement uncertainty as already de-

scribed above in Section S1.1.

S2 Measurement statistics

The left panel of Figure S1 (a, c, e) shows the number of data points used to calculate the concentration of CO, O_3, and their ratio for each grid box, available from the twelve campaign data sets used in this study. Note that before averaging, each data set had a different time resolution and therefore already represents an average of different time resolutions onto 60 s (see Table 2 in main study). On the right side of Figure S1 (b, d, f), the standard errors of the means relative to the mean (RSEM) in percent are displayed for CO, O_3 and their ratio, respectively. The RSEM is given by:

$$\text{RSEM} = \frac{\frac{\sigma}{\sqrt{N}}}{mean} \times 100, \tag{S1}$$

with the standard deviation σ, the number per grid cell N, and the $mean$ of each grid cell. The RSEM provides a variability of the averaged measurements relative to the mean value of each grid cell. Note that this also includes atmospheric and seasonal variability in averaging all campaigns. However, when RSEM is small ($<5\%$), and counts are high (≥ 10), the observations show very good agreement throughout all data sets. This is the case, for example, in the tropical upper troposphere, where seasonal variability is small. For regions with stronger seasonal variability, e. g., at the tropopause, RSEM is higher ($\leq 15\%$), even if there is a high number of counts per grid cell. Conversely, small RSEM with small counts per grid cell, e. g., in the southern polar latitudes and southern subtropics, show regions with small variability, but averages from only a few flights through this area, which neglects annual variability. Therefore, we decided to categorize the data set using two conditions to show statistical relevant data, with a sufficient number of counts per grid cell ($N \geq 10$) and a reasonable variability of the mean values (RSEM $\leq 15\%$). This has been indicated using hatching in Figure 2 in the main study.

The highest RSEM and therefore the strongest variability between the campaign data sets is found in the vicinity to the tropopause, especially for O_3 (Fig. S1, d). We attribute this to the different altitudes of the tropopause throughout the years and the different campaigns. Especially close to the tropopause, the gradient of O_3 is very steep, with increasing O_3 towards the stratosphere, and therefore leads to such high variability. However, as we are focusing on the troposphere and filter out mixing ratios higher than 100 ppbv of O_3, following Prather et al. (2011)), these differences have a negligible effect on our results. In the RSEM of CO, only a few grid points show very large percentages above 15%. Those can be linked to extreme events (e. g., biomass burning), which were measured during single measurement campaigns and increase the standard deviation.

S3 Comparison of observations with model

To test the statistical representativeness of the observations, the model was compared with the observations (Figure S2). For this, the flight tracks were extracted on a 1-hour resolution from the monthly climatology of the model, following a nearest point algorithm. The extracted data has been binned with a zonal resolution of 10° and a vertical resolution of 2 km. This flight track extraction is an interpolation and should give worse results for comparison between the model and the observations. Taking this into account, there is good agreement between the model-generated climatological data and the flight track extracted data of the model across the troposphere. This confirms that there is sufficient observational data for our analysis, and the selected campaigns are considered statistically representative. In the southern hemisphere, however, the difference between "mod" and "ft mod" becomes larger from 6 km upwards, which shows that there is not enough observational data to represent the climatology of the southern hemisphere mid- to upper troposphere. However, this supports the focus on the northern hemisphere in the main study.

Comparing the full model and the observations in Figure S2, they are mostly in agreement in the lower troposphere and free troposphere. Towards the tropopause, there seems to be an increased overestimation of the model. Here, the model overestimates mainly O_3, as for CO the comparison looks better (not shown here). Nevertheless, as this comparison is following just a nearest point algorithm based on hourly data, a direct comparison should approximate the data. However, this comparison is

sufficient for the scope of this work and allows us to confidently use the whole model data for the $O_3 - CO$ ratio analysis of the northern subtropics, the sensitivity study, and representing the observations.

S4 Global zonal gradients

In Figure S3 the global 10° and 2 km averaged zonal gradients for CO, O_3, and their ratio are shown for the observations ((a), (b), (c)), the model ((d), (e), (f)) and the sensitivity model run ((g), (h), (i)). The smaller number of observations available for the southern hemisphere mean that this study was focused on the northern hemisphere. Nevertheless, the observations and the model show a good agreement in the CO values on the southern hemisphere, while O_3 seems to be overestimated by the model, mostly in the upper troposphere. This overestimation of O_3 could be identified also in the study of Jöckel et al. (2016). A subtropical enhancement of the $O_3 - CO$ ratio in the southern hemisphere can be seen by the model, but it is not as clear in the observations. Besides the lack of data for the southern hemisphere, this can be due to the difference in the chemical background concentrations prevailing in the southern mid- to high latitudes. As the Hadley circulation and its transport from the tropics into the subtropics is similar in both hemispheres, stratosphere–troposphere mixing processes might be different due to less land cover, stronger zonal winds, and less vertical exchange processes, as there are less obstacles. Therefore, mixing with the stratosphere is less pronounced as is the seasonal cycle of total stratospheric mass exchange (Appenzeller et al., 1996). The overestimation of O_3 in the upper troposphere in the model might be an indicator of an overestimation of STE in the model or the representation of the right tropopause height. Furthermore, the southern extra tropics contain the cleanest air on Earth, due to the lower population, cities, biomass burning, land cover, and ship traffic. CO background mixing ratios in the southern hemisphere is 60 ppbv and O_3 mixing ratios is 30 ppbv at the surface, both being lower than in the northern hemispheric extra tropics, where CO varies from 100 – 140 ppbv and O_3 from 30 – 45 ppbv (Fig. S3, (a), (b)). Especially for CO, there is no increase in surface emissions towards the southern higher latitudes. All those factors contribute to the less pronounced enhancement of the $O_3 - CO$ ratio in the southern subtropics, as we could identify in the northern subtropics.

The sensitivity run of the model excludes all lightning emissions from the simulation. As discussed in the main study, this results in generally higher CO, and lower O_3 mixing ratios globally as well as less variation in the tracers in the vertical column of the troposphere. This is also the case for the southern hemisphere, which can be seen in the lowest panel of Figure S3 and in the annual zonal distribution in Figure S4. Thus, in terms of $O_3 - CO$ ratios, the hemispheres are almost identical. In the northern hemisphere, there is generally more lightning than in the southern hemisphere due to the larger land cover (Schumann and Huntrieser, 2007). Nevertheless, in the southern hemisphere, the background values are much lower, and other causes of high $O_3 - CO$ ratios are much less important (i.e., stratosphere–troposphere mixing), hence the absolute and relative differences of excluding LNO_x are generally stronger in the southern hemisphere than in the northern. The absolute and relative difference in the $O_3 - CO$ ratio including and excluding LNO_x is by a factor of two larger in the southern hemisphere than in the northern hemisphere (Fig. S5).

S4.1 Seasonal variability

Figures S6, S7, S8, S9, S10, and S11 show monthly zonal distributions of CO, O_3, and $O_3 - CO$ ratios from the standard simulation and the sensitivity run excluding LNO_x from the EMAC model. A strong seasonality can be seen for both CO and O_3. Maximum CO emissions are modeled in the boreal winter, while O_3 mixing ratios are found in the boreal summer in the northern hemisphere. This influences also the $O_3 - CO$ ratio in the subtropics in both hemispheres, peaking in the summer months and being weakest during winter (Fig. S10). By excluding LNO_x emissions (Fig. S11) the $O_3 - CO$ ratios generally decline, resulting in a much more homogeneous troposphere than when lightning emissions are included. Nevertheless, the maximum increase in the subtropical $O_3 - CO$ ratio can still be noted in the summer, stronger in the northern than in the southern hemisphere, which makes other factors responsible for the strong seasonality.

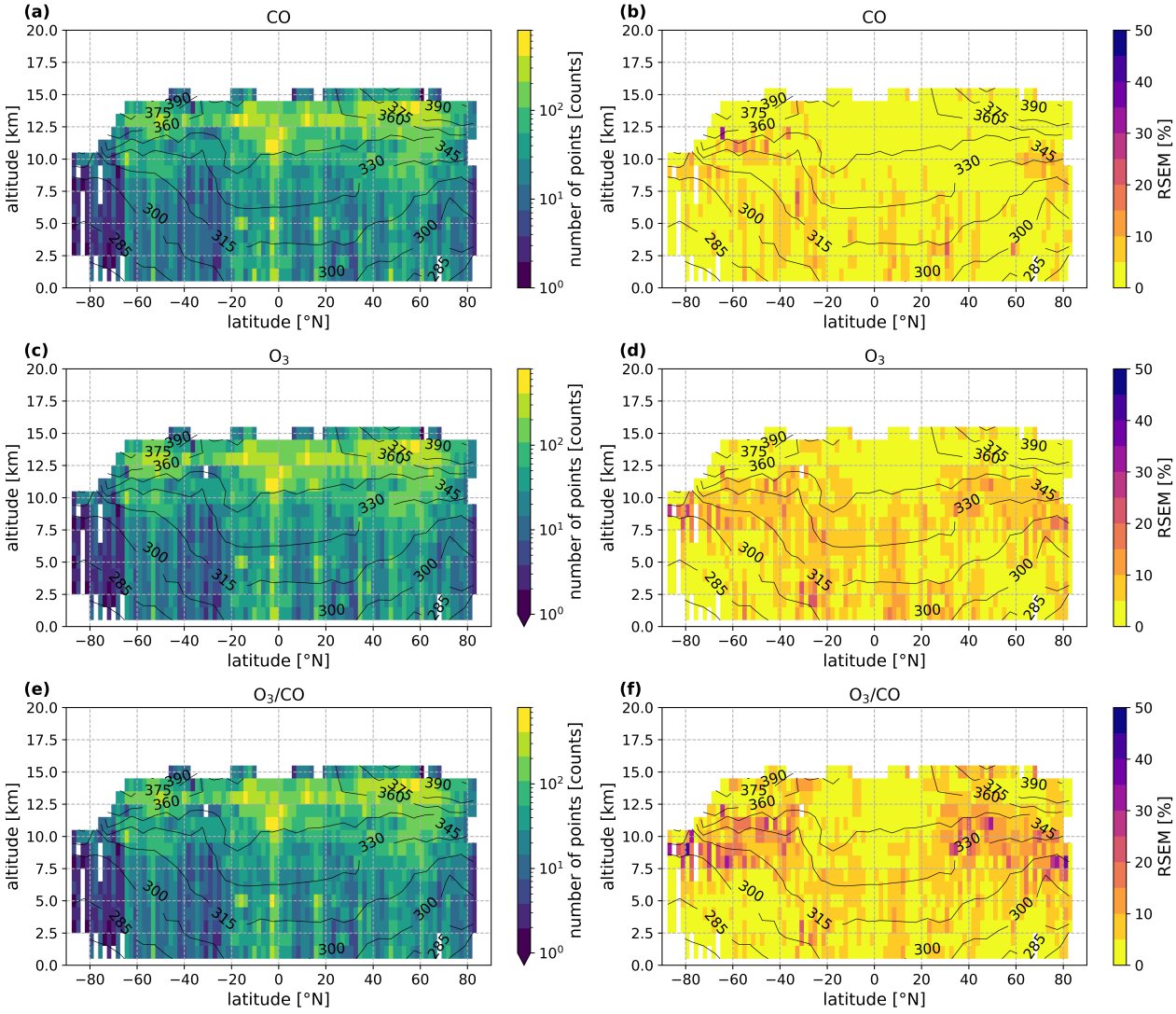

Figure S1. Zonal distribution of CO (a, b), O_3 (c, d), and their ratio (e, f) showing the number of data points per grid cell and the standard error of the mean relative to the mean (RSEM) in percent, calculated via Eq. 1, respectively. Black lines indicate layers of constant potential temperature, averaged over 5° and 1 km.

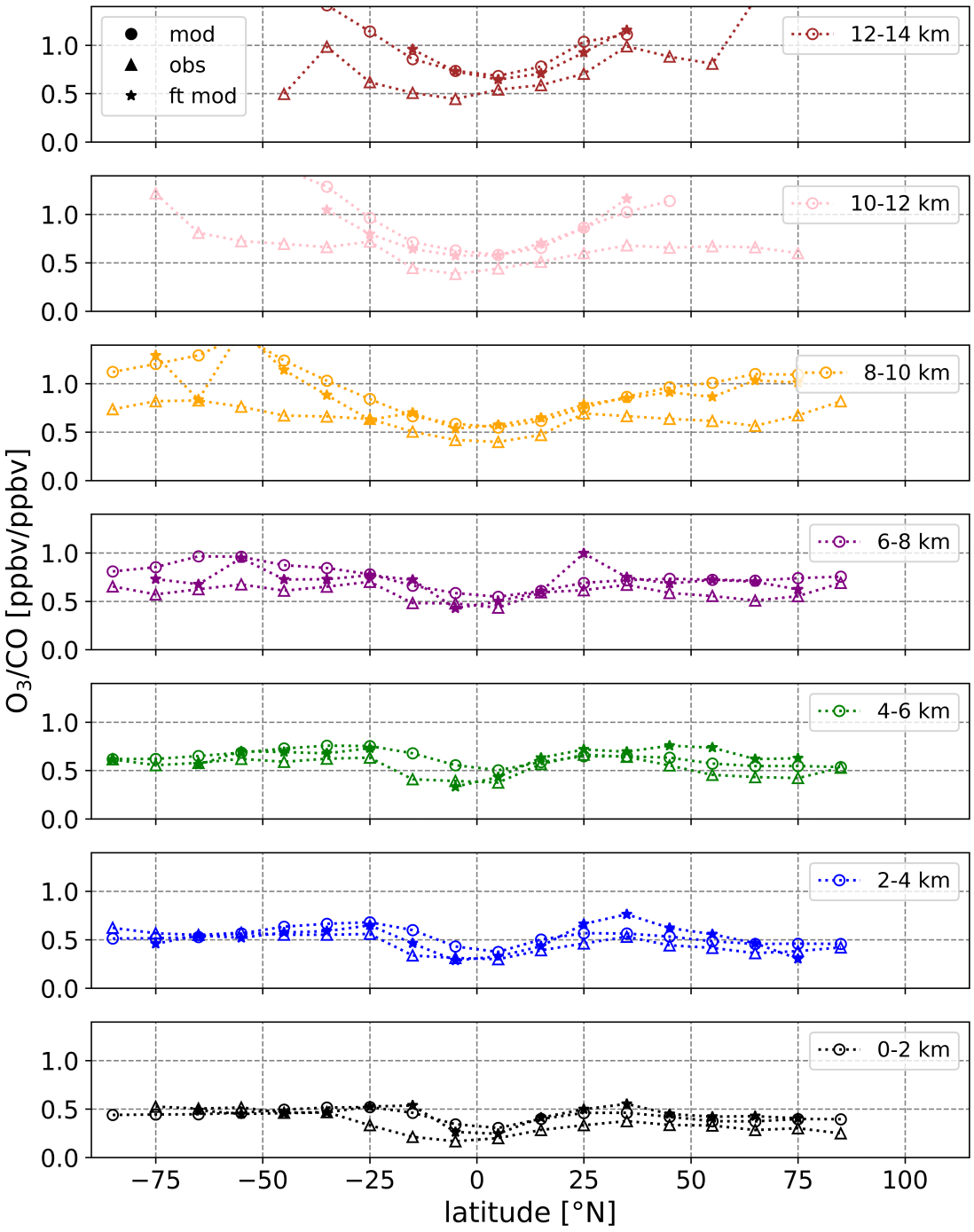

Figure S2. Comparison of the model climatology (mod, circles), observations (obs, triangles), and the model sampled along the flight tracks (ft mod, stars). Displayed are the zonal medians averaged over 10° and 2 km. Before the calculations, stratospheric values were filtered out by excluding all data points with O_3 mixing ratios higher than 100 ppbv, according to Prather et al. (2011).

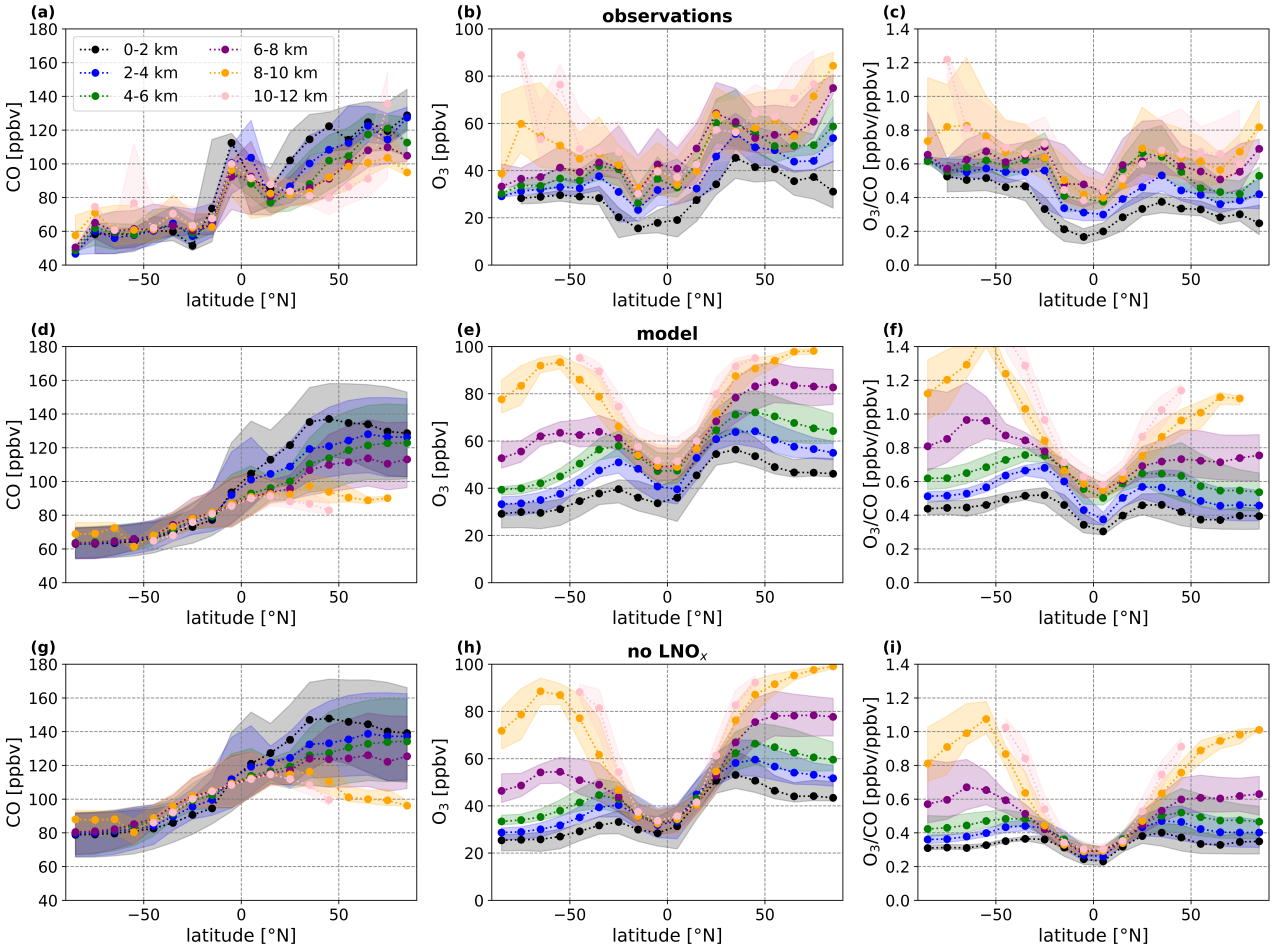

Figure S3. Global zonal gradients of the observations, the model, and the sensitivity run, excluding LNO_x for CO ((a), (d), (g)), O_3 ((b), (e), (h)), and their ratio ((c), (f), (i)), respectively. The gradients represent the zonal median values with the 25th and 75th percentiles as shaded areas from averages of 10° of latitude, and 2 km of altitude. Before the calculations, stratospheric values were filtered out by excluding all data points with O_3 mixing ratios higher than 100 ppbv, according to Prather et al. (2011).

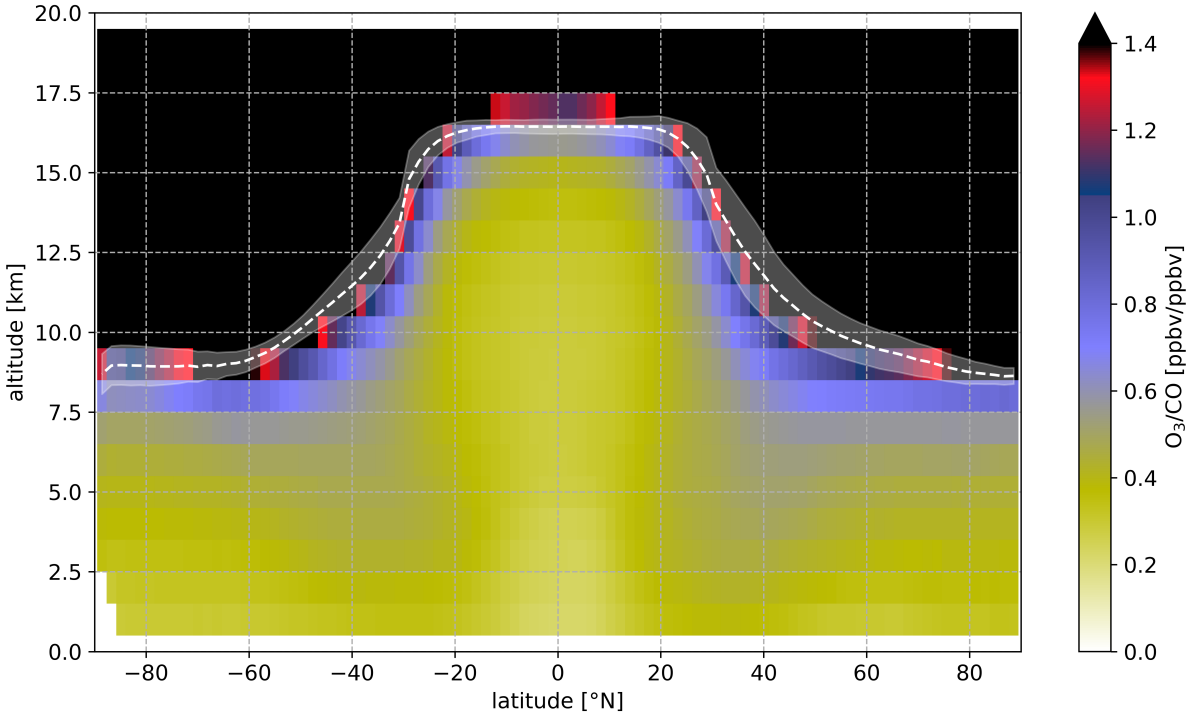

Figure S4. The median annual zonal distribution of the sensitivity simulation, excluding LNO_x for the ratio between O_3 and CO. All data points are averaged over 1 km altitude and 1.875° latitude. The scale has been adjusted to display tropospheric values. The white dashed line indicates the tropopause height and the standard deviation is shaded in white.

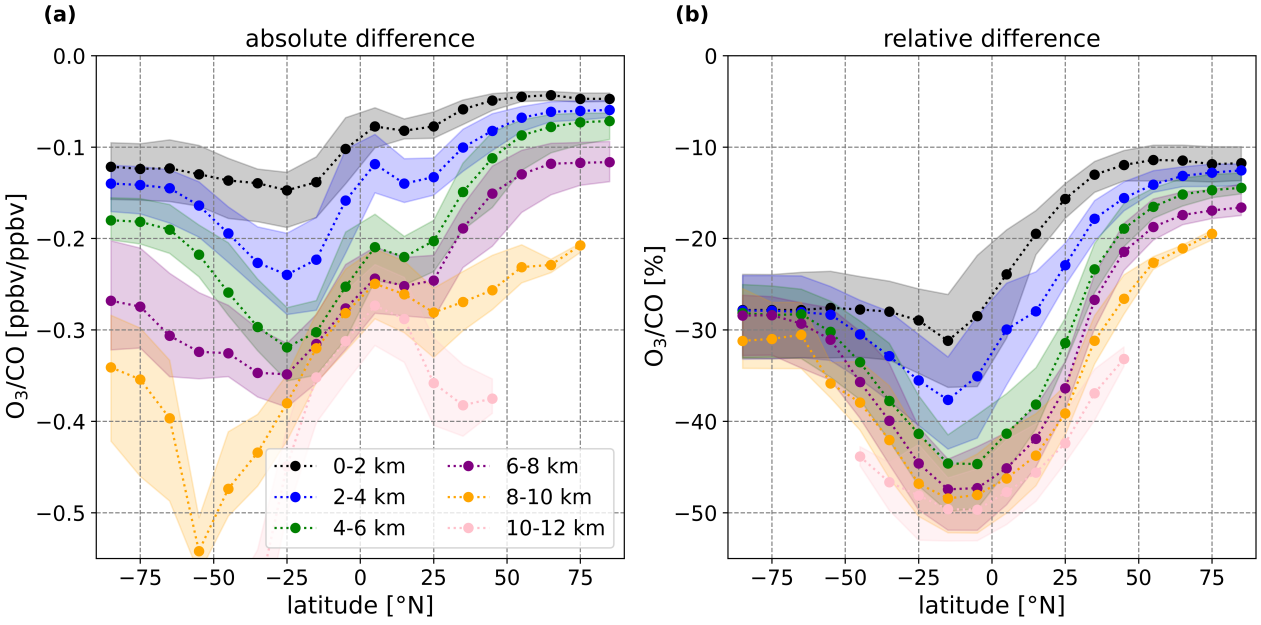

Figure S5. Modeled global zonal gradients of the absolute (a) and the relative (b) difference of the standard simulation and the sensitivity run excluding LNO_x, created by the EMAC model, averaged over all longitudes, 10° of latitude, and 2 km of altitude. Dots represent medians as dots and the 25th and 75th percentiles are represented as shaded areas. Before the calculations, stratospheric values were filtered out by excluding all data points above 100 ppbv of O_3, according to Prather et al. (2011). The calculation of the relative and absolute differences can be found in the main study.

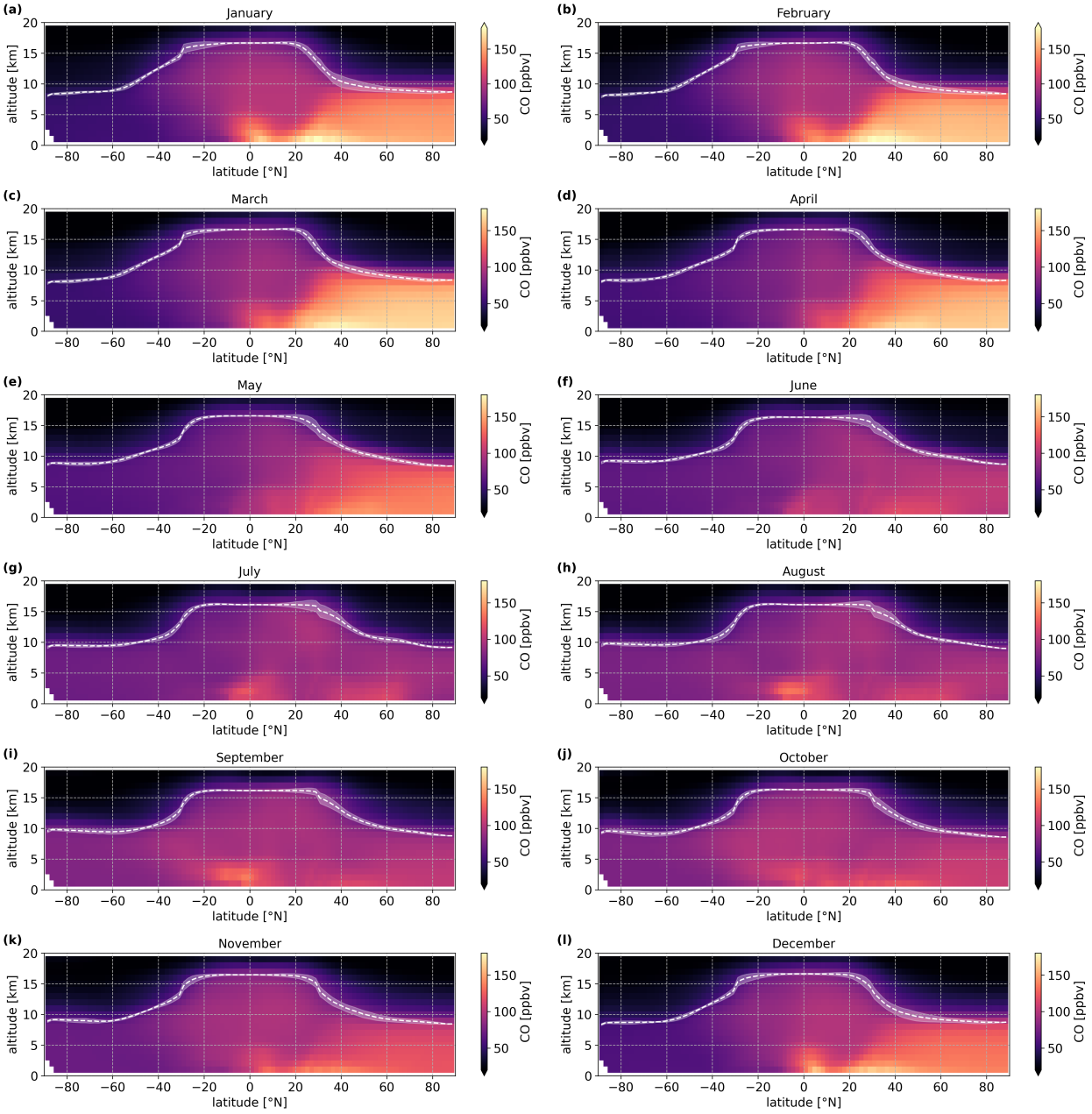

Figure S6. Modeled global zonal distributions of CO over all months including January (a), February (b), March (c), April (d), May (e), June (f), July (g), August (h), September (i), October (j), November (k), and December (l), created by the EMAC model data (standard simulation), averaged over all longitudes, 1 km of altitude, and 1.875° of latitude. Displayed are the mean values. The scale has been adjusted to represent tropospheric values. The white dotted line represents the height of the tropopause with standard deviation derived by averaging over the longitudes.

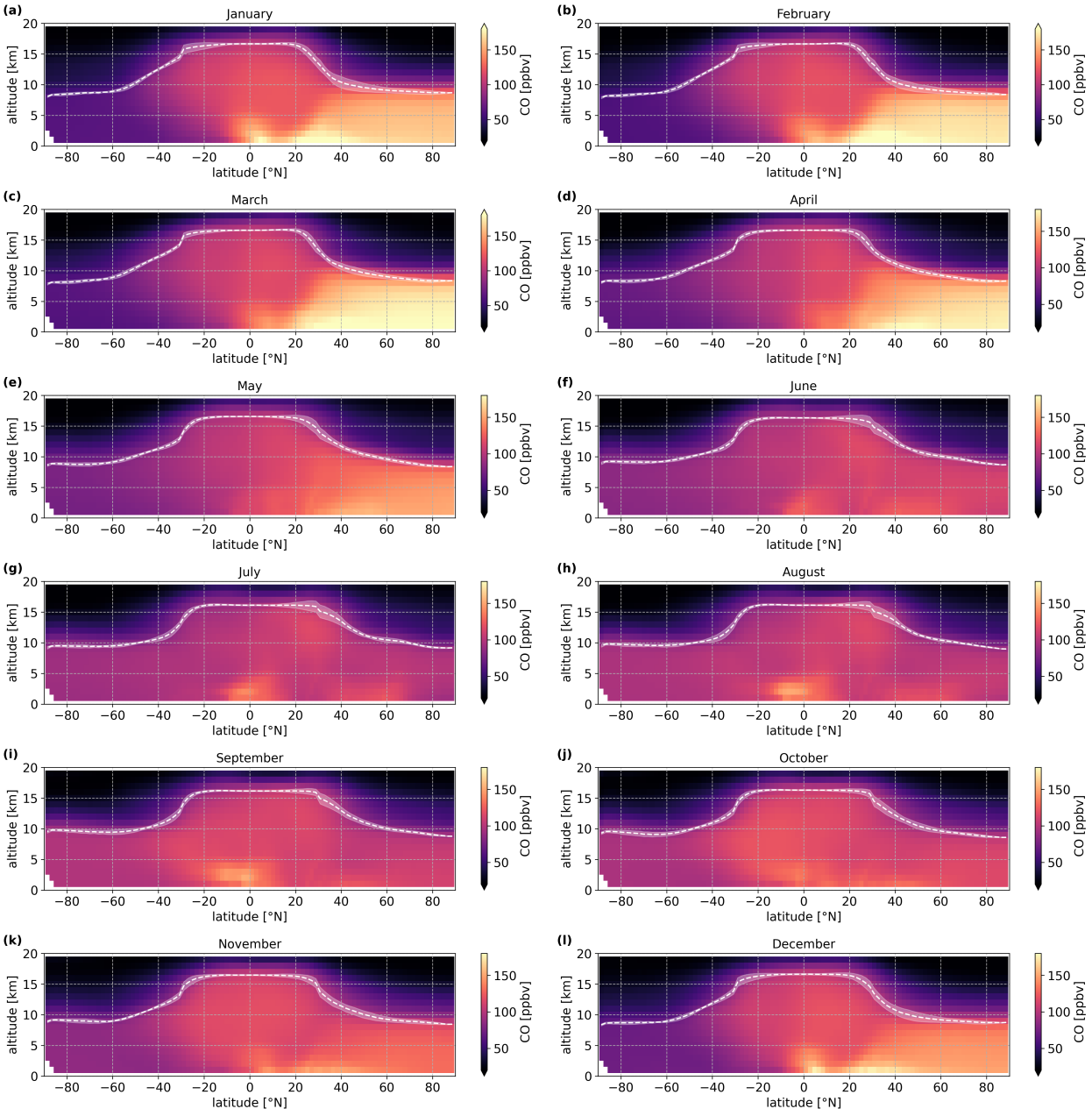

Figure S7. Same as Figure S6, for the sensitivity run excluding LNO_x.

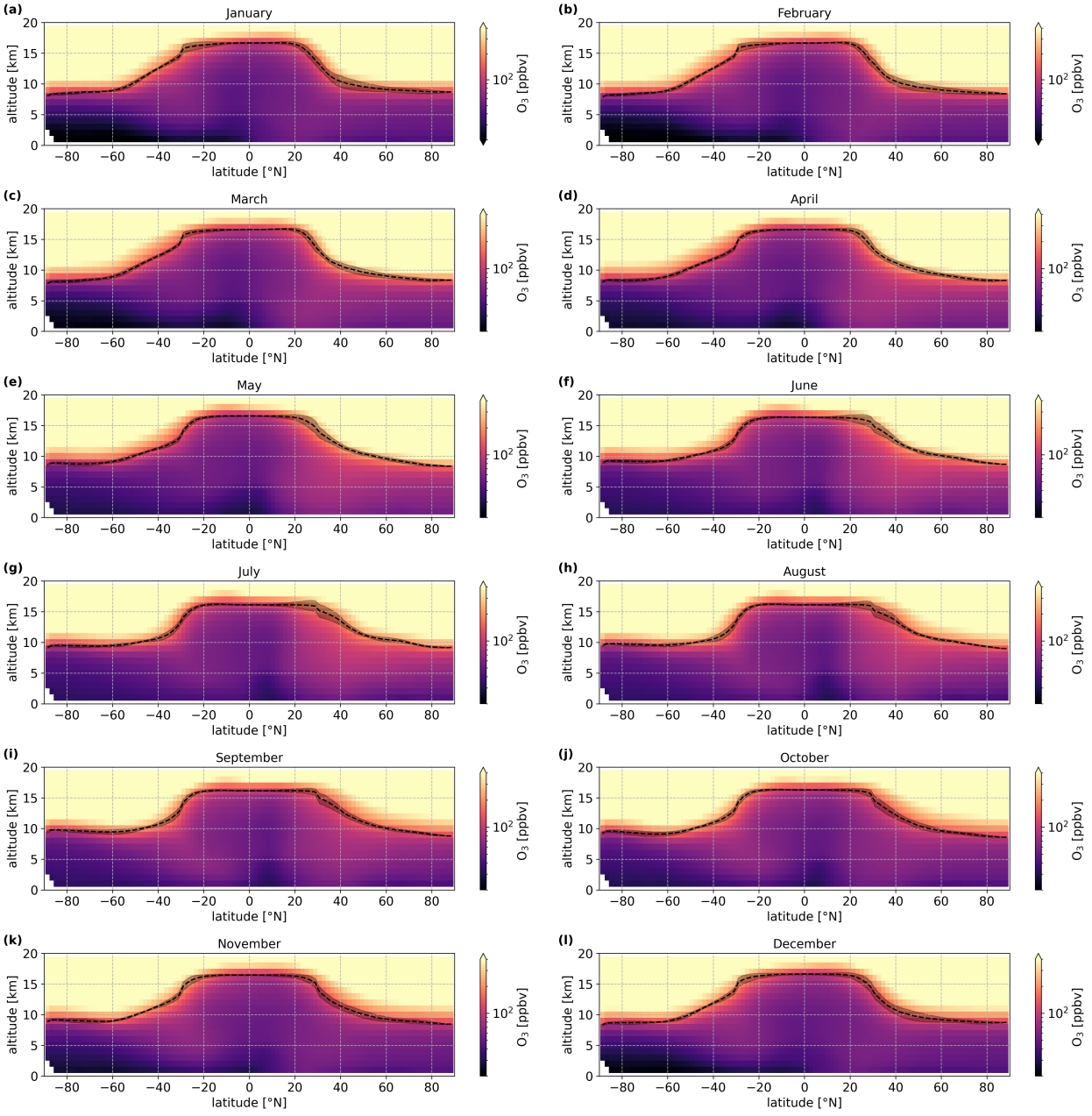

Figure S8. Modeled global zonal distributions of O_3 over all months including January (a), February (b), March (c), April (d), May (e), June (f), July (g), August (h), September (i), October (j), November (k), and December (l), created by the EMAC model data (standard simulation), averaged over all longitudes, 1 km of altitude, and 1.875° of latitude. Displayed are the mean values. The scale has been adjusted to represent tropospheric values. The black dotted line represents the height of the tropopause with standard deviation derived by averaging over the longitudes.

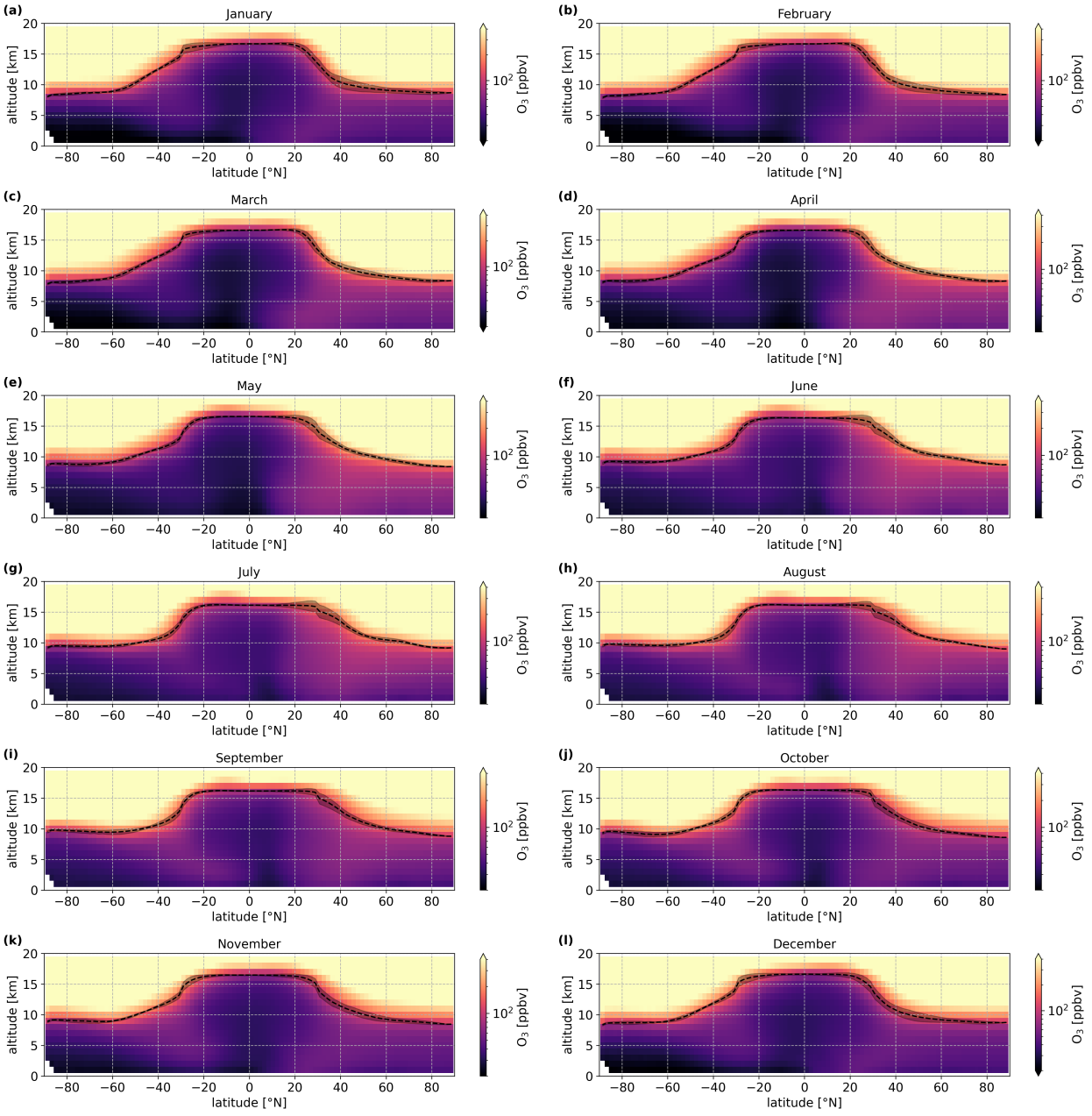

Figure S9. Same as Figure S8, for the sensitivity run excluding LNO_x.

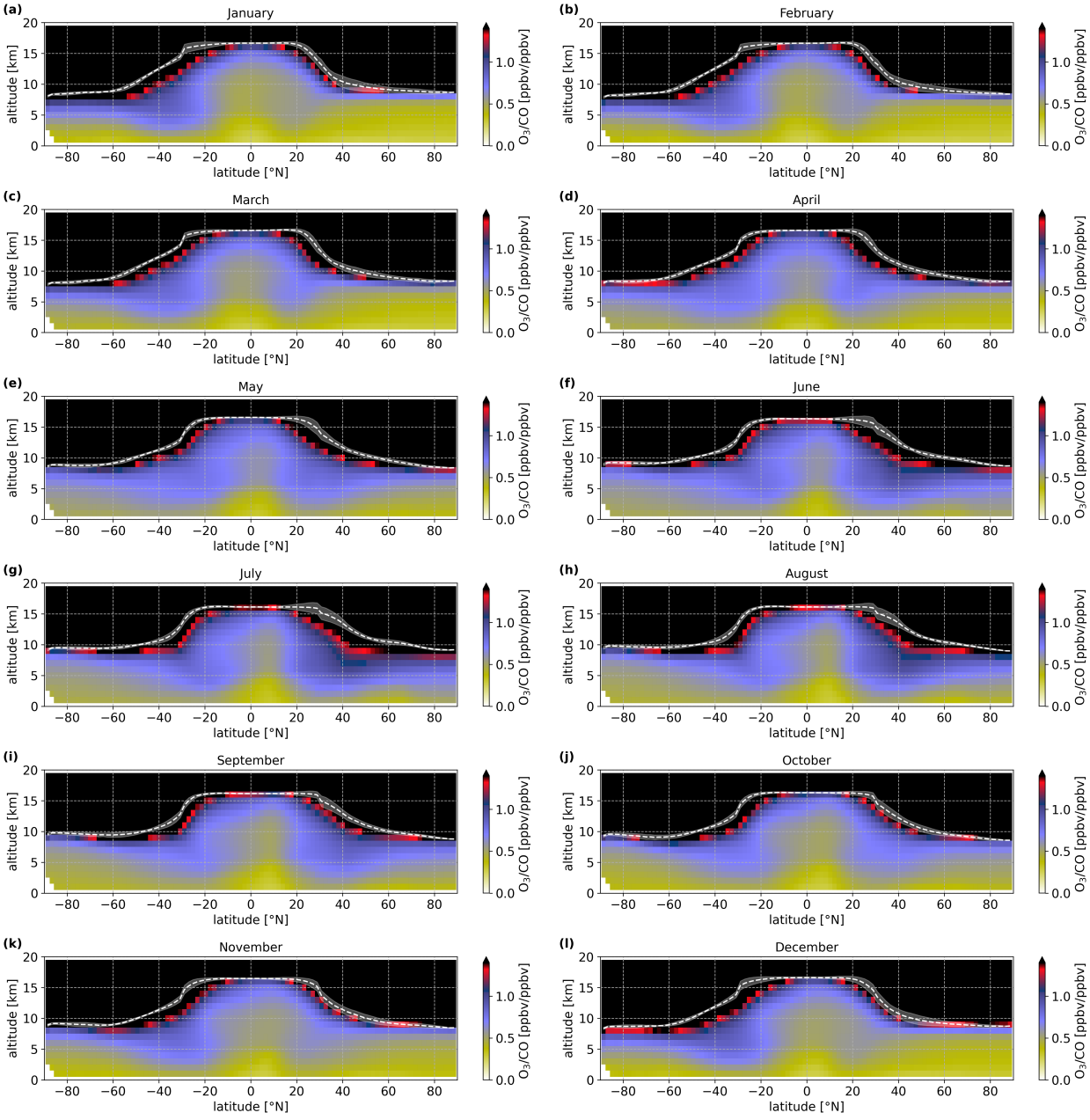

Figure S10. Modeled global zonal distributions of the O_3 – CO ratio of the sensitivity run without LNO_x over all months including January (a), February (b), March (c), April (d), May (e), June (f), July (g), August (h), September (i), October (j), November (k), and December (l), created by the EMAC model data (standard simulation), averaged over all longitudes, 1 km of altitude, and 1.875° of latitude. Displayed are the mean values. The scale has been adjusted to represent tropospheric values. The white dotted line represents the height of the tropopause with standard deviation derived by averaging over the longitudes.

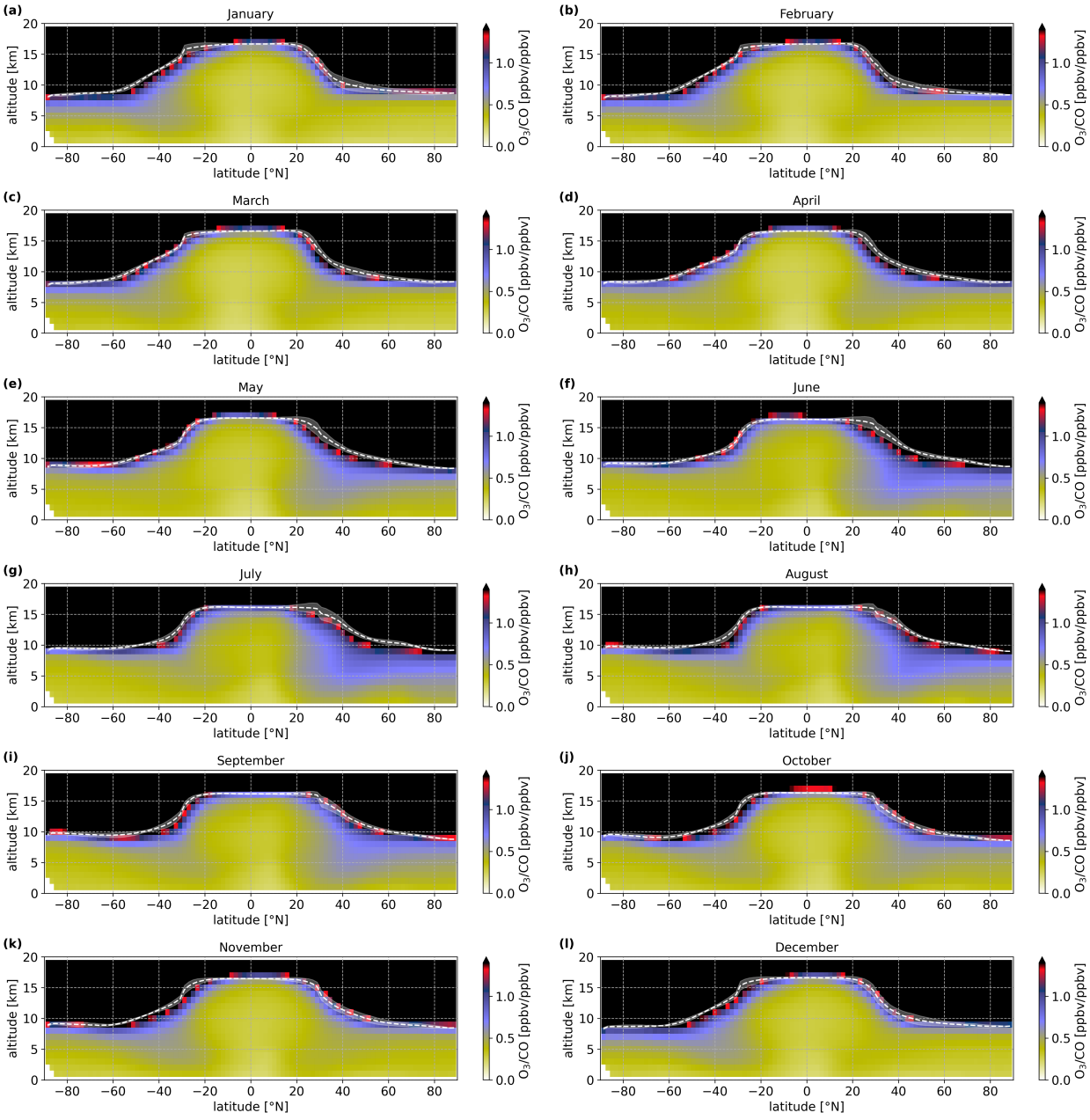

Figure S11. Same as Figure S10, for the sensitivity run excluding LNO_x.

References

Appenzeller, C., Holton, J. R., and Rosenlof, K. H.: Seasonal variation of mass transport across the tropopause, Journal of Geophysical Research: Atmospheres, 101, 15 071–15 078, https://doi.org/https://doi.org/10.1029/96JD00821, 1996.

Bartolome Garcia, I., Spang, R., Ungermann, J., Griessbach, S., Krämer, M., Höpfner, M., and Riese, M.: Observation of cirrus clouds with GLORIA during the WISE campaign: detection methods and cirrus characterization, Atmospheric Measurement Techniques, 14, 3153–3168, https://doi.org/10.5194/amt-14-3153-2021, 2021.

Bourgeois, I., Peischl, J., Thompson, C. R., Aikin, K. C., Campos, T., Clark, H., Commane, R., Daube, B., Diskin, G. W., Elkins, J. W., Gao, R.-S., Gaudel, A., Hintsa, E. J., Johnson, B. J., Kivi, R., McKain, K., Moore, F. L., Parrish, D. D., Querel, R., Ray, E., Sánchez, R., Sweeney, C., Tarasick, D. W., Thompson, A. M., Thouret, V., Witte, J. C., Wofsy, S. C., and Ryerson, T. B.: Global-scale distribution of ozone in the remote troposphere from the ATom and HIPPO airborne field missions, Atmospheric Chemistry and Physics, 20, 10 611–10 635, https://doi.org/10.5194/acp-20-10611-2020, 2020.

Bourgeois, I., Peischl, J., Neuman, J. A., Brown, S. S., Thompson, C. R., Aikin, K. C., Allen, H. M., Angot, H., Apel, E. C., Baublitz, C. B., Breweri, J. F., Campuzano-Josta, P., Commane, R., Crounse, J. D., Daube, B. C., DiGangi, J. P., Diskin, G. S., Emmons, L. K., Fiore, A. M., Gkatzelis, G. I., Hills, A., Hornbrook, R. S., Huey, L. G., Jimenez, J. L., Kim, M., Lacey, F., McKain, K., Murray, L. T., Nault, B. A., Parrish, D. D., Ray, E., Sweeney, Colmand Tanner, D., Wofsy, S. C., and Ryerson, T. B.: Large contribution of biomass burning emissions to ozone throughout the global remote troposphere, Proceedings of the National Academy of Sciences, 118, e2109628 118, https://doi.org/10.1073/pnas.2109628118, 2021.

Chiu, R., Obersteiner, F., Franchin, A., Campos, T., Bailey, A., Webster, C., Zahn, A., and Volkamer, R.: Intercomparison of fast airborne ozone instruments to measure eddy covariance fluxes: spatial variability in deposition at the ocean surface and evidence for cloud processing, Atmospheric Measurement Techniques, 17, 5731–5746, https://doi.org/10.5194/amt-17-5731-2024, 2024.

DLR: HALO data, base, ESMVal mission [data set], https://halo-db.pa.op.dlr.de/mission/14, last access: 18 June 2024, 2012.

DLR: HALO data base, OMO mission [data set], https://halo-db.pa.op.dlr.de/mission/0, last access: 18 June 2024, 2015.

DLR: HALO data, base, WISE mission [data set], https://halo-db.pa.op.dlr.de/mission/96, last access: 18 June 2024, 2017.

DLR: HALO data, base, CAFE Africa [data set], https://halo-db.pa.op.dlr.de/mission/98, last access: 18 June 2024, 2018.

DLR: HALO data, base, SouthTRAC mission [data set], https://halo-db.pa.op.dlr.de/mission/116, last access: 18 June 2024, 2019.

DLR: HALO data, base, CAFE Brazil [data set], https://halo-db.pa.op.dlr.de/mission/135, last access: 18 June 2024, 2023a.

DLR: HALO data, base, PHILEAS mission [data set], https://halo-db.pa.op.dlr.de/mission/138, last access: 18 June 2024, 2023b.

DLR: HALO data, base, CAFE Pacific [data set], https://halo-db.pa.op.dlr.de/mission/140, last access: 23 December 2024, 2024.

Hottmann, B., Hafermann, S., Tomsche, L., Marno, D., Martinez, M., Harder, H., Pozzer, A., Neumaier, M., Zahn, A., Bohn, B., et al.: Impact of the South Asian monsoon outflow on atmospheric hydroperoxides in the upper troposphere, Atmospheric chemistry and physics, 20, 12 655–12 673, https://doi.org/10.5194/acp-20-12655-2020, 2020.

Jöckel, P., Tost, H., Pozzer, A., Kunze, M., Kirner, O., Brenninkmeijer, C. A. M., Brinkop, S., Cai, D. S., Dyroff, C., Eckstein, J., Frank, F., Garny, H., Gottschaldt, K.-D., Graf, P., Grewe, V., Kerkweg, A., Kern, B., Matthes, S., Mertens, M., Meul, S., Neumaier, M., Nützel, M., Oberländer-Hayn, S., Ruhnke, R., Runde, T., Sander, R., Scharffe, D., and Zahn, A.: Earth system chemistry integrated modelling (ESCiMo) with the modular earth submodel system (MESSy) version 2.51, Geoscientific Model Development, 9, 1153–1200, https://doi.org/10.5194/gmd-9-1153-2016, 2016.

Krasauskas, L., Ungermann, J., Preusse, P., Friedl-Vallon, F., Zahn, A., Ziereis, H., Rolf, C., Ploeger, F., Konopka, P., Vogel, B., and Riese, M.: 3-D tomographic observations of Rossby wave breaking over the Northern Atlantic during the WISE aircraft campaign in 2017, Atmospheric Chemistry and Physics Discussions, 2020, 1–30, https://doi.org/10.5194/acp-21-10249-2021, 2020.

Kunkel, D., Hoor, P., Kaluza, T., Ungermann, J., Kluschat, B., Giez, A., Lachnitt, H.-C., Kaufmann, M., and Riese, M.: Evidence of small-scale quasi-isentropic mixing in ridges of extratropical baroclinic waves, Atmospheric Chemistry and Physics, 19, 12 607–12 630, https://doi.org/10.5194/acp-19-12607-2019, 2019.

McManus, J. B., Zahniser, M. S., Jr., D. D. N., Shorter, J. H., Herndon, S. C., Wood, E. C., and Wehr, R.: Application of quantum cascade lasers to high-precision atmospheric trace gas measurements, Optical Engineering, 49, 111 124, https://doi.org/10.1117/1.3498782, 2010.

Müller, S., Hoor, P., Berkes, F., Bozem, H., Klingebiel, M., Reutter, P., Smit, H., Wendisch, M., Spichtinger, P., and Borrmann, S.: In situ detection of stratosphere-troposphere exchange of cirrus particles in the midlatitudes, Geophysical research letters, 42, 949–955, https://doi.org/10.1002/2014GL062556, 2015.

Müller, S., Hoor, P., Bozem, H., Gute, E., Vogel, B., Zahn, A., Bönisch, H., Keber, T., Krämer, M., Rolf, C., et al.: Impact of the Asian monsoon on the extratropical lower stratosphere: trace gas observations during TACTS over Europe 2012, Atmospheric chemistry and physics, 16, 10 573–10 589, https://doi.org/10.5194/acp-16-10573-2016, 2016.

Ort, L., Röder, L. L., Parchatka, U., Königstedt, R., Crowley, D., Kunz, F., Wittkowski, R., Lelieveld, J., and Fischer, H.: In-flight characterization of a compact airborne quantum cascade laser absorption spectrometer, Atmospheric Measurement Techniques, 17, 3553–3565, https://doi.org/10.5194/amt-17-3553-2024, 2024.

Prather, M. J., Zhu, X., Tang, Q., Hsu, J., and Neu, J. L.: An atmospheric chemist in search of the tropopause, Journal of Geophysical Research: Atmospheres, 116, https://doi.org/https://doi.org/10.1029/2010JD014939, 2011.

Rapp, M., Martin, R., Sinnhuber, B.-M., Hoor, P., and Engel, A.: SouthTRAC mission website, https://www.pa.op.dlr.de/southtrac/home/science/scientific-objectives/, last access: 13 June 2024, 2019.

Rapp, M., Kaifler, B., Dörnbrack, A., Gisinger, S., Mixa, T., Reichert, R., Kaifler, N., Knobloch, S., Eckert, R., Wildmann, N., Giez, A., Krasauskas, L., Preusse, P., Geldenhuys, M., Riese, M., Woiwode, W., Friedl-Vallon, F., Sinnhuber, B.-M., de la Torre, A., Alexander, P., Hormaechea, J. L., Janches, D., Garhammer, M., Chau, J. L., Conte, J. F., Hoor, P., and Engel, A.: SOUTHTRAC-GW: An airborne field campaign to explore gravity wave dynamics at the world's strongest hotspot, Bulletin of the American Meteorological Society, 102, E871–E893, https://doi.org/10.1175/BAMS-D-20-0034.1, 2021.

Ridley, B., Grahek, F., and Walega, J.: A small high-sensitivity, medium-response ozone detector suitable for measurements from light aircraft, Journal of Atmospheric and Oceanic Technology, 9, 142–148, https://doi.org/10.1175/1520-0426(1992)009<0142:ASHSMR>2.0.CO;2, 1992.

Riese, M., K. M. and Hoor, P.: WISE: project description, https://www.halo.dlr.de/science/missions/wise/wise.html, last access: 15 July 2024, 2017.

Röder, L. L., Ort, L., Lelieveld, J., and Fischer, H.: Quantitative analysis of temporal stability and instrument performance during field experiments of an airborne QCLAS via Allan–Werle-plots, Applied Physics B, 130, 118, https://doi.org/10.1007/s00340-024-08254-5, 2024.

Rolf, C., Afchine, A., Bozem, H., Buchholz, B., Ebert, V., Guggenmoser, T., Hoor, P., Konopka, P., Kretschmer, E., Müller, S., Schlager, H., Spelten, N., Suminska-Ebersoldt, O., Ungermann, J., Zahn, A., and Krämer, M.: Transport of Antarctic stratospheric strongly dehydrated air into the troposphere observed during the HALO-ESMVal campaign 2012, Atmospheric chemistry and physics, 15, 9143–9158, https://doi.org/10.5194/acp-15-9143-2015, 2015.

Santoni, G., Daube, B. C., Kort, E., Jiménez, R., Park, S., Pittman, J., Gottlieb, E., Xiang, B., Zahniser, M., Nelson, D., et al.: Evaluation of the airborne quantum cascade laser spectrometer (QCLS) measurements of the carbon and greenhouse gas suite–CO 2, CH 4, N 2 O, and CO–during the CalNex and HIPPO campaigns, Atmospheric Measurement Techniques, 7, 1509–1526, https://doi.org/10.5194/amt-7-1509-2014, 2014.

Schiller, C., Bozem, H., Gurk, C., Parchatka, U., Königstedt, R., Harris, G., Lelieveld, J., and Fischer, H.: Applications of quantum cascade lasers for sensitive trace gas measurements of CO, CH_4, N_2O and HCHO, Applied Physics B, 92, 419–430, https://doi.org/10.1007/s00340-008-3125-0, 2008.

Schumann, U. and Huntrieser, H.: The global lightning-induced nitrogen oxides source, Atmospheric Chemistry and Physics, 7, 3823–3907, https://doi.org/10.5194/acp-7-3823-2007, 2007.

Strode, S. A., Liu, J., Lait, L., Commane, R., Daube, B., Wofsy, S., Conaty, A., Newman, P., and Prather, M.: Forecasting carbon monoxide on a global scale for the ATom-1 aircraft mission: insights from airborne and satellite observations and modeling, Atmospheric Chemistry and Physics, 18, 10 955–10 971, https://doi.org/10.5194/acp-18-10955-2018, 2018.

Tadic, I., Parchatka, U., Königstedt, R., and Fischer, H.: In-flight stability of quantum cascade laser-based infrared absorption spectroscopy measurements of atmospheric carbon monoxide, Applied Physics B, 123, 1–9, https://doi.org/10.1007/s00340-017-6721-z, 2017.

Tadic, I., Nussbaumer, C. M., Bohn, B., Harder, H., Marno, D., Martinez, M., Obersteiner, F., Parchatka, U., Pozzer, A., Rohloff, R., et al.: Central role of nitric oxide in ozone production in the upper tropical troposphere over the Atlantic Ocean and western Africa, Atmospheric Chemistry and Physics, 21, 8195–8211, https://doi.org/10.5194/acp-21-8195-2021, 2021.

Thompson, C. R., Wofsy, S. C., Prather, M. J., Newman, P. A., Hanisco, T. F., Ryerson, T. B., Fahey, D. W., Apel, E. C., Brock, C. A., Brune, W. H., Froyd, K., Katich, J. M., Nicely, J. M., Peischl, J., Ray, E., Veres, P. R., Wang, S., Allen, H. M., Asher, E., Bian, H., Blake, D., Bourgeois, I., Budney, J., Bui, T. P., Butler, A., Campuzano-Jost, P., Chang, C., Chin, M., Commane, R., Correa, G., Crounse, J. D., Daube, B., Dibb, J. E., DiGangi, J. P., Diskin, G. S., Dollner, M., Elkins, J. W., Fiore, A. M., Flynn, C. M., Guo, H., Hall, S. R., Hannun, R. A., Hills, A., Hintsa, E. J., Hodzic, A., Hornbrook, R. S., Huey, L. G., Jimenez, J. L., Keeling, R. F., Kim, M. J., Kupc, A., Lacey, F., Lait, L. R., Lamarque, J.-F., Liu, J., McKain, K., Meinardi, S., Miller, D. O., Montzka, S. A., Moore, F. L., Morgan, E. J., Murphy, D. M., Murray, L. T., Nault, B. A., Neuman, J. A., Nguyen, L., Gonzalez, Y., Rollins, A., Rosenlof, K., Sargent, M., Schill, G., Schwarz, J. P., Clair, J. M. S., Steenrod, S. D., Stephens, B. B., Strahan, S. E., Strode, S. A., Sweeney, C., Thames, A. B., Ullmann, K., Wagner, N., Weber, R., Weinzierl, B., Wennberg, P. O., Williamson, Christina J. amd Wolfe, G. M., and Zeng, L.: The NASA Atmospheric Tomography (ATom) mission: Imaging the chemistry of the global atmosphere, Bulletin of the American Meteorological Society, 103, E761–E790, https://doi.org/10.1175/BAMS-D-20-0315.1, 2022.

Tomsche, L., Pozzer, A., Ojha, N., Parchatka, U., Lelieveld, J., and Fischer, H.: Upper tropospheric CH 4 and CO affected by the South Asian summer monsoon during the Oxidation Mechanism Observations mission, Atmospheric Chemistry and Physics, 19, 1915–1939, https://doi.org/10.5194/acp-19-1915-2019, 2019.

White, J. U.: Optical system providing a long optical path, last access: 24 June 2024, uS Patent 2,779,230, 1957.

Wienhold, F., Fischer, H., Hoor, P., Wagner, V., Königstedt, R., Harris, G., Anders, J., Grisar, R., Knothe, M., Riedel, W., Libken, F.-J., and Schilling, T.: TRISTAR-A tracer in-situ TDLAS for atmospheric research, Applied Physics B, 67, 411–417, https://doi.org/10.1007/s003400050524, 1998.

Wofsy, S., Afshar, S., Allen, H., Apel, E., Asher, E., Barletta, B., Bent, J., Bian, H., Biggs, B., Blake, D., et al.: ATom: Merged atmospheric chemistry, trace gases, and aerosols, ORNL DAAC, https://doi.org/10.3334/ORNLDAAC/1581, 2018.

Zahn, A., Weppner, J., Widmann, H., Schlote-Holubek, K., Burger, B., Kühner, T., and Franke, H.: A fast and precise chemiluminescence ozone detector for eddy flux and airborne application, Atmospheric Measurement Techniques, 5, 363–375, https://doi.org/https://doi.org/10.5194/amt-5-363-2012, 2012.